Improving UAV-SfM photogrammetry for measurement of high-relief terrain: image collection strategies and ground control quantity

Abstract: Image collection strategies and ground control points (GCPs) are of particular importance for UAV–SfM photogrammetry, and the generalization of their effects has proved elusive. This study designed various photogrammetric scenarios to investigate the effects of image collection strategies, ground control quantity, and their interaction on digital elevation model (DEM) errors and their spatial structure in high-relief terrain. The results of 1.77×10^5 UAV–SfM scenarios provide insights for improving UAV-SfM practices. A high image capture angle (20°- 40°) enhances camera calibration quality decreasing the magnitude and spatial correlation of errors. High camera inclination reduces the sensitivity of mean and standard deviation of error to flying height, but not the spatial correlation of error. Including additional data (e.g., supplemented convergent images; images captured at multiple flying heights) has only a minor effect if imagery is highly inclined. GCPs provide more effective constraints than image collection strategies. The mean error and standard error decline quickly with a small number of GCPs and then become stable in all scenarios, but the spatial

correlation of error can be further improved with increasing GCPs. However, the effects of GCP quantity do interact with image collection strategies. High camera inclination reduces requirements for GCPs, while strategies combining different flying heights and image orientations have little effect on necessary GCP quantity. The distribution of GCPs still affects the errors, but the effect of GCP distribution becomes less important with an increase in the number of GCPs. Finally, we show that UAV-SfM photogrammetric quality assessment should routinely assess the spatial dependence of error using a statistic like Moran's I.
Keywords: UAV-SfM photogrammetry; Terrain modeling; Oblique photography; Ground control points; Combination datasets

1 Introduction

Uncrewed aerial vehicles (UAVs) combined with Structure-from-Motion (SfM) and Multi-View Stereoscopic (MVS) photogrammetric workflows have proven to be capable of producing high-resolution (centimeter-level) orthoimages and digital elevation models (DEMs) at low cost (Eltner et al., 2015; Harwin and Lucieer, 2012; Hugenholtz et al., 2013; Ouedraogo et al., 2014), including over rugged topography and in hardly accessible areas. Recent UAV–SfM applications in geomorphological research notably include terrain modelling (e.g., James et al., 2020; Hugenholtz et al., 2013; Rosnell and Honkavaara, 2012), topographic change detection (Eltner et al., 2015; Lane et al., 2020; Meinen and Robinson, 2020;: Roncoroni et al., 2023) and the quantification of mass movements (e.g. Niethammer et al., 2010; Turner et al., 2015).

There is a general consensus that UAV–SfM can be effective and accurate for terrain modeling provided basic design guidelines are followed (e.g. James et al., 2020); but that deeper considerations of image collection and ground control are required for improving accuracy (associated with systematic error or bias) and precision (describing random error) in high relief landforms (Agueera-Vega et al., 2018; Carvajal-Ramírez et al., 2016; Nieminski and Graham, 2017), such as gully slopes and sub-vertical cliffs. The accuracy and precision in UAV-SfM terrain modeling depend on a range of factors including: camera properties (camera lens, image resolution), image collection strategies (flying height, flying speed, stability, number and overlapping of images, camera angle), image quality (light, contrast, shadows, blurring), terrain texture, and the number and distribution of ground control points (GCPs) (Escobar Villanueva et al., 2019; Polat and Uysal, 2018; Sanz‐Ablanedo et al., 2020). Among these factors, image collection strategies, and ground control quantity and distribution have been identified as of particular importance, and can be controlled by operators (James et al., 2019; James et al., 2017a).

Image collection strategies for UAV–SfM are different from conventional airborne photogrammetry. Conventional airborne photogrammetry tended to use metric cameras, which have reliable camera calibrations. As use of this imagery does not require camera calibration image can be acquired at a constant altitude, with sufficient overlap (along- and cross-strip) and nadir image capture (Wolf et al., 2014). Even then, these datasets can produce some systematic error, revealed when digital elevation data from different dates are compared for stable zones, but the error is commonly small in magnitude, a linear function of horizonal coordinates and easily removed (e.g. Westaway et al., 2003; Bakker and Lane, 2017). This is not the case with consumer-grade UAVs. These are mostly equipped with non-metric cameras, with unknown internal camera parameters, significant image distortion and unstable calibration (Harwin et al., 2015; James and Robson, 2014) that have to be determined after data collection. To increase the view of the scene and to improve the quality of the scene reconstruction, oblique photography is generally recommended UAVs (James et al., 2020; Jiang et al., 2017; Rossi et al., 2017) although some studies (e.g. James et al., 2020) suggest we should move beyond 'off-nadir' imagery. Theoretically, four oblique and one nadir-facing cameras are ideal for oblique photography (Adams et al., 2014; Toth and Jóźków, 2016). However, most consumer-grade, low-cost UAVs are equipped with a camera that can only view a single direction during surveys. Hence, flights with a "double grid" pattern (consisting of two orthogonal blocks) with an inclined camera have been widely used in studies using a (James et al., 2020; Nesbit and Hugenholtz, 2019; Roncoroni et al., 2022). Besides camera inclination angle, combination datasets, such as nadir image blocks supplemented with convergent images and the combinations of images captured at different flying heights (Meinen and Robinson, 2020; Sanz-Ablanedo et al., 2020), have been proposed for improving UAV-SfM terrain modeling. However, there is still no consensus on optimal camera angles for these different image collection strategies and it may be that optimal configurations are specific to individual applications.

In addition to image collection strategies, ground control points (GCP) appear to be crucial for improving UAV-SfM photogrammetry (James et al., 2020). Ground control has two substantial functions: georeferencing UAV-SfM models on the one hand, and reducing both random and systematic errors during the photogrammetric bundle adjustment on the other hand (James et al., 2017a; James et al., 2017b). The accuracy, number, and distribution of GCPs are key factors (Padró et al., 2019; Rangel et al., 2018). The accuracy of GCPs is mainly controlled by the precision of the measurement instrument (e.g., dGPS, total station), while the number and distribution of GCPs can be flexibly arranged in practice, when surveyed terrains are accessible.

In terms of the distribution of GCPs, a general consensus within the community recommends the combination of a stratified distribution of GCPs within the surveyed scene, with beyond-scene GCPs to provide additional support during the bundle adjustment (Cabo et al., 2021; Rangel et al., 2018; Stott et al., 2020). In terms of the number of GCPs, an improvement in accuracy and precision of the reconstructed scene is observable with an increasing number of GCPs, until a certain threshold beyond which adding more GCPs does not improve the model quality any further (James et al., 2017a; Martínez-Carricondo et al., 2018a; Rangel et al., 2018). The requirements in terms of GCP number and distribution also vary according to the type of scene surveyed (e.g. texture, relief; James et al. 2017a; 2020). Although previous studies have individually investigated the effects of image collection strategies (Nesbit and Hugenholtz, 2019) and ground control quantity (Cabo et al., 2021; James et al., 2017a), the interactive effects of image collection strategies and ground control quantity are less considered.

In this contribution, we investigate the interactive effects of image collection strategies and ground control quantity on terrain modelling errors and their spatial structure in UAV-SfM surveys, by comparing more than 1.77×10^5 scenarios with various combinations of camera angles, flight heights, nadir and/or oblique imagery, and different number and distribution of GCPs (Fig. 1). We also introduce a new method for determining the extent of spatial structure in error fields by using a spatial autocorrelation statistic, Moran's I. According to the accuracy, precision, and spatial structure of errors of the derived DEMs, this paper aims at synthetizing recommendations for improving UAV SfM-MVS practices in high landscape relief.

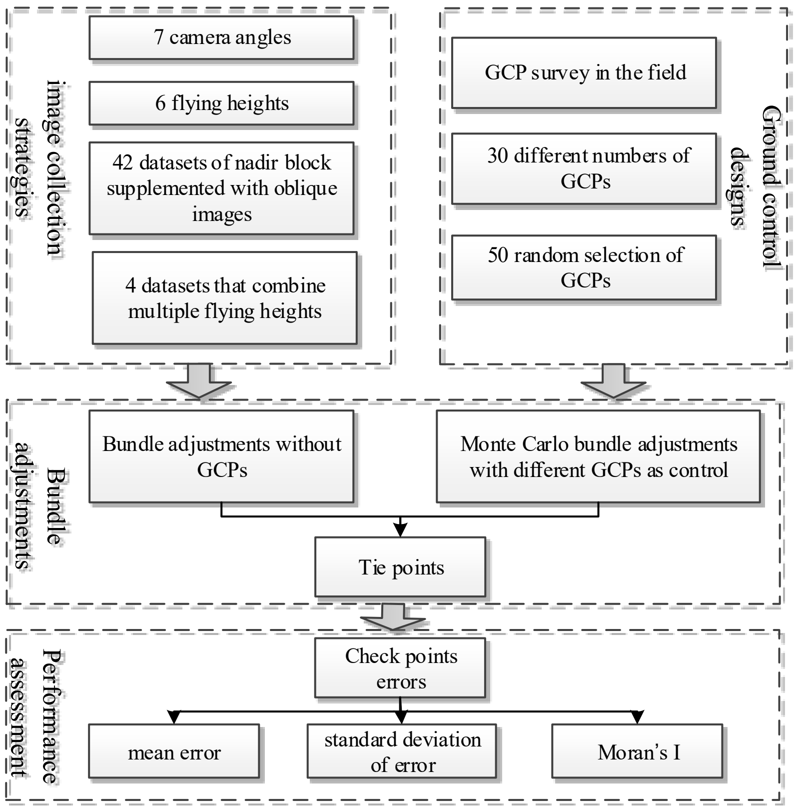

Figure 1. Flowchart of the processes and analyses.

2 Methodology

2.1 Study sites

The work was conducted in the Loess Plateau of China, a region associated with severe and active gully erosion (Dai et al., 2022; Dai et al., 2019), resulting in high relief topography. This research focused on two study areas in Shaanxi province; T1 (110°17′3.2″E, 37°33′48.8″N, 5.1 ha in size) and T2 (110°21′45.7″E, 37°35′12.8″N, 3.6 ha in size), in Suide county. The study sites have high mean slope (~23°) and hence high relief (~100 m maximum elevation difference) (Fig. 2 a and b). These areas are covered with grassland and the vegetation is very sparse in winter and spring, which facilitates UAV-SfM photogrammetry.

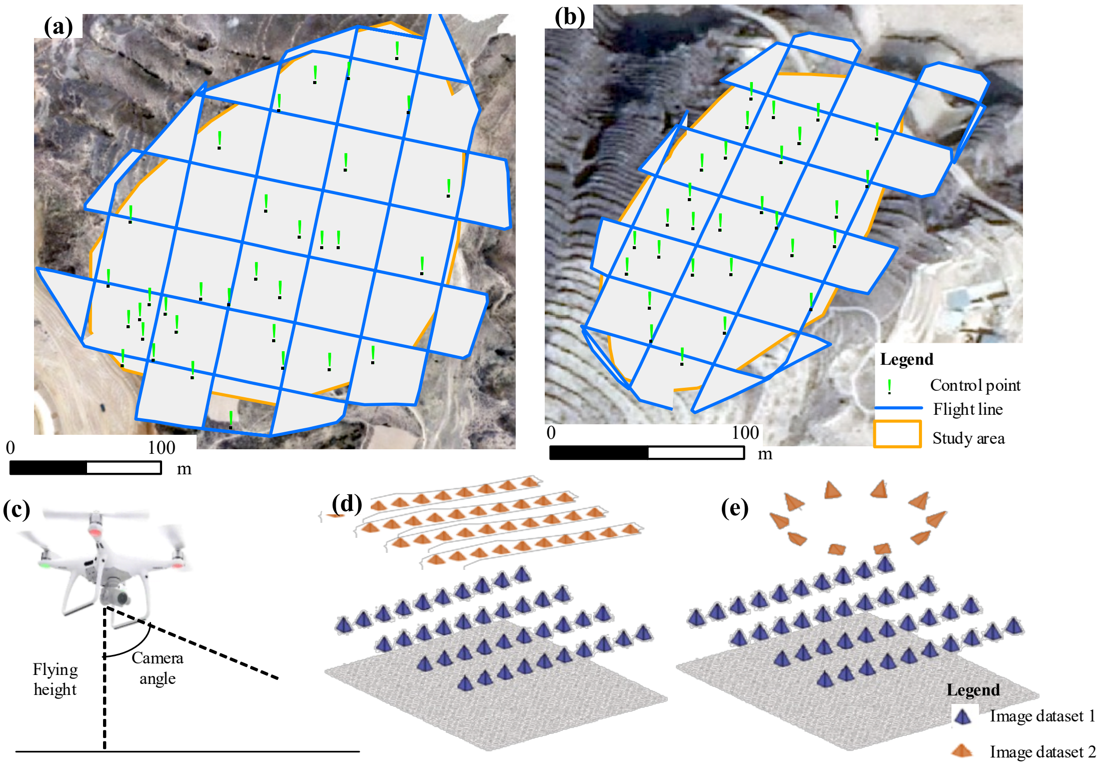

Figure 2. Study areas and flight design: (a) and (b) are orthoimages and 'double-grid' designs in the T1, T2 areas, respectively; (c) is diagram of camera angle and flying height; (d)and (e) are diagrams of multiple flight height blocks and nadir image blocks supplemented with convergent images, respectively.

2.2 Image acquisition

A DJI Phantom 4 Pro quadcopter was used in this study due to its low cost, its flying stability and the ease with which flights are programmed (e.g., James et al., 2020). It was mounted with a 1" CMOS camera with a 24-mm focal length (35 mm equivalent). The on-board GNSS precision of this UAV was ±1.5 m (horizontal) and ±0.5 m (vertical). Due to the low on-board GNSS precision and the need for self-calibration of the camera, an optimized image collection strategy and ground control are generally needed (James et al., 2020).

We collected the UAV images in March 2021. In this season, vegetation has not yet grown in the study areas, which means that very few areas were masked during the flights (Fig. 2). Given the aim of the paper, we explored different strategies for UAV image acquisition.

First, to investigate the effect of camera angle on survey precision and accuracy, the camera angle was varied from 0 to 40° (0° indicating a nadir inclination) within individual surveys. Given that camera angles higher than 40° would lead to greater observation distances than the flying height, we did not set a higher camera angle. The drone rotates through 180° at the end of each strip, which means that with an angle of 10°, the camera angle is actually +10° in one line and -10° in the next strip. During the flights, to minimize the effects of other flight factors, we set the same flying height (defined by the elevation of the take-off point, which was held constant in between surveys), flight path and overlap rate for all UAV surveys. By setting the flying height as constant from the take-off point, but flying the UAV horizontally over a steep terrain, different image capture heights result.

The image collection comprised two orthogonal blocks (‘double-grid’) (Fig. 2a and b), with an 80% overlap both along- and cross-strip. Due to the high relief, the UAV flights were started halfway up the mountain in each study area. The average flight height and average ground sample distance (GSD) ranged from 70 to 100 m and 1.9 to 2.7 cm, respectively, for the two study areas (Table 1).

Table 1. The experiment of different camera angle

Study areas	**Camera angle (°)**	**Number of images for each flight**	**Flight height (m)**	**GSD (cm)**
T1	0, 5, 10, 20, 30, 35, 40	~200	100	2.7
T2	0, 5, 10, 20, 30, 35, 40	~120	70	1.9

Second, we designed a flying height experiment, with the flying heights set from 60 to 160 m (because we expect the required GSD is less than 5 cm for monitoring gully erosion), with the same 80% image overlap. To investigate whether the camera angle interacts with flying height, we repeated the flights with both a nadir camera and a 15° inclined camera in the T1 and T2 areas, respectively (Table 2).

Table 2. The experiments with different flight height

Study areas	**Flight height (m)**	**Number of images for each flight**	**Camera angle (°)**	**GSD(cm)**
T1	60, 80, 100, 120, 140, 160	110 ~ 300	0	1.6 - 4.4
T2	60, 80, 100, 120, 140, 160	70 ~ 140	15	1.6 - 4.4

These data allowed us to construct and to test the effects of different combination datasets (Fig. 2c and 2d). First, we added in supplemented convergent imagery (Fig. 2d) given its potential importance for reducing systematic error in DEMs derived using SfM-MVS photogrammetry (James et al., 2020). Here, a nadir or off-nadir double-grid block was supplemented with several additional convergent images. We called the double-grid blocks (nadir or off-nadir) as main blocks. The main blocks used were the same as those in Table 1. The supplemented convergent images with camera angles from 0° to 40° were collected at 120 m and 80 m flying heights in the T1 and T2 areas (Table 3), respectively. Each supplemented convergent dataset includes 16 photos. Then, we supplied the bundle adjustment with different combinations of the main blocks and supplementary convergent images (Table 3).

Multiple flying heights have been also suggested to improve UAV-SfM applications in previous studies (James and Robson, 2014). To analyze how the number of combined flying heights affects precision and accuracy, we designed image combinations with 2, 4, and 6 flying heights, and kept the mean flight height to be the same (Table 4). This experiment also allowed demonstration of effects of interactions between camera angle and flying height, and so we set a nadir camera and 15° inclined camera in the T1 and T2 areas, respectively.

Table 3. The strategies of "main block + supplemented images"

Dataset No.	**Main block (°)**		**supplemented images (°)**	
	Camera angle (°)	**Flight height(m)**	**Camera angle (°)**	**Flight height(m)**
1	0		0	
2	0		5	
3	0		10	
4	0		20	
5	0		30	
6	0		35	
7	0		40	
8	5		0	
9	5		5	
10	5	T1 area: 100	10	T1 area: 110
11	5	T2 area: 70	20	T2 area: 80
12	5		30	
13	5		35	
14	5		40	
…	…		…	
43	40		0	
44	40		5	
45	40		10	
46	40		20	
47	40		30	

48	40	35
49	40	40

Table 4. The experiment of combinations with different flying height

Study area	Camera angle(°)	No.1 Two heights(m)	No.2 Four heights (m)	No.3 Six heights (m)
T1	0	100, 120	80, 100, 120, 140,	60, 80, 100, 120, 140, 160
T2	15	100, 120	80, 100, 120, 140,	60, 80, 100, 120, 140, 160

2.3 Ground control points

We distributed 33 and 31 ground control points (GCPs) in the T1 and T2 (Figure 2), respectively. The GCPs were deployed at peaks, ridges, and gully bottoms in each study area to ensure that their distribution is even in both low and high points of the topography (Figure 2). They comprised 1 m × 1 m black and white targets (Figure 3). The control point (target center) is clearly visible at up to 200 m flight height. All GCPs were surveyed by a Topcon Hiper SR GNSS-RTK. The horizontal and vertical accuracy for GCPs surveyed with GNSS-RTK were ±0.010 m and ±0.015 m, respectively.

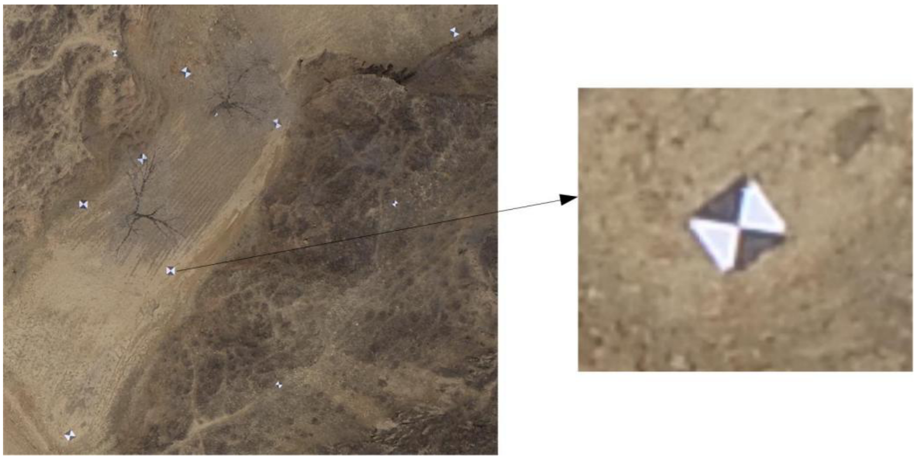

Figure 3. The target used for ground control points

2.4 Data processing

We applied two data processing procedures to investigate the performance of the image collection strategies: GCP-free and GCP-constrained. In the GCP-free scenario, we mainly focus on the effect of image collection strategies. Hence, we use only two

GCPs to shift, to rotate, and to scale tie points and hence the acquired topographic data and imagery. The remaining GCPs were used as check points for accuracy assessment. Here, an issue arose: different selection of two GCPs affected the georeferencing. To model the uncertainty of georeferencing, we randomly selected two GCPs 50 times and then used a boxplot to show how tie point accuracy changes.

Previous studies (James et al., 2020) showed that poorly designed flight plans may lead to unwanted correlations between parameters of the camera model, which can generate systematic error in derived DEMs. Here, to further understand this effect, we evaluated the correlation of camera calibration parameters to see how it changes with camera angle in the GCP-free scenario.

The GCP-constrained scenario used GCPs to improve the bundle adjustment. Previous research (Cabo et al., 2021; Tonkin and Midgley, 2016; Villanueva and Blanco, 2019) has shown that continuous increases of GCP quantity had only a limited impact on photogrammetric accuracy when the GCP coverage reaches a certain density. We labelled "optimal number" the number of GCPs beyond which no significant improvement in point cloud accuracy and precision is reached. To investigate whether different image collection strategies affect the photogrammetric accuracy, we employed two Monte Carlo GCP experiments (James et al., 2017a). First, for each Monte Carlo realization, the same number (x) of GCPs was selected to optimize the bundle adjustment, and the rest of the GCPs were used as check points to assess the accuracy. The process was then repeated 50 times with a different random selection of GCPs. Second, for each Monte Carlo realization, the partitioning between optimizing GCPs and check GCPs was varied, with a gradual increase in the percentage (10% in steps of 10% to 90%) of GCPs randomly selected. The Monte Carlo GCP tests were carried out in the Agisoft PhotoScan Pro 1.5 and using the Python code (James et al., 2017a).

With the image collection, ground control, and data processing strategies used, more than 1.77×10^5 scenarios were processed in this study (2 study areas × (7 camera angles + 6 flying height + 42 datasets of nadir block supplemented with oblique images + 4 datasets that combine multiple flying heights) × 30 different numbers of GCPs × 50 random selections of GCPs). This large number of simulations allowed the interactions between image collection strategies and ground control quantity to be accessed.

2.5 Performance assessment

In this study, we focus on the elevation error (Z error) for terrain modeling. We used two standard metrics, the mean error (ME) as a representation of systematic error; and the standard deviation of error (STD) as a measure of precision (Nesbit and Hugenholtz, 2019). The main problem with these quantitative measures is that they do not consider the extent to which error is spatially variable, a commonly reported finding when DEMs of difference are calculated and "doming" or "dishing" is apparent. For this reason, we also quantified the extent to which there is a spatial structure to the error. We used the Moran's I (Moran, 1950) for this purpose (Eq. (1)). Moran's I lies between -1 and 1. The closer its value to 1 or -1, the more positive or negative the spatial autocorrelation of errors, respectively. A value of 0 indicates a random distribution of error in space:

$$Moran's\ I = \frac{n}{S_o} \cdot \frac{\sum_{i=1}^{n}\sum_{j=1}^{n} w_{i,j}(x_i-\bar{x})(x_j-\bar{x})}{\sum_{i=1}^{n}(x_i-\bar{x})^2} \quad (1)$$

where n is the number of spatial units indexed by i and j; x is the variable of interest; $\bar{x}$ is the mean of x; $w_{i,j}$ is a matrix of spatial weights with zeroes on the diagonal; and S_o is the sum of all $w_{i,j}$. Clearly, a goal for an effective image calibration is that the Moran's I statistic is not significantly different from that associated with a spatially random distribution of error.

3 Results

3.1 Effects of single camera angle

3.1.1 Effects of single camera angle without GCPs

The effect of a single camera angle on the ME and the STD is presented in Fig.4. As the camera angle increases, the ME and STD show the same global trend which becomes smaller at first and then stable when the camera angle is bigger than 10°. This indicates that an inclined camera is beneficial to improve both accuracy and precision in this case, but that very high inclined angles may be unnecessary according to the stabilization in ME and STD. However, the sensitivity to choice of GCPs is reduced at greater camera angles (the uncertainty ranges become smaller, Fig.4).

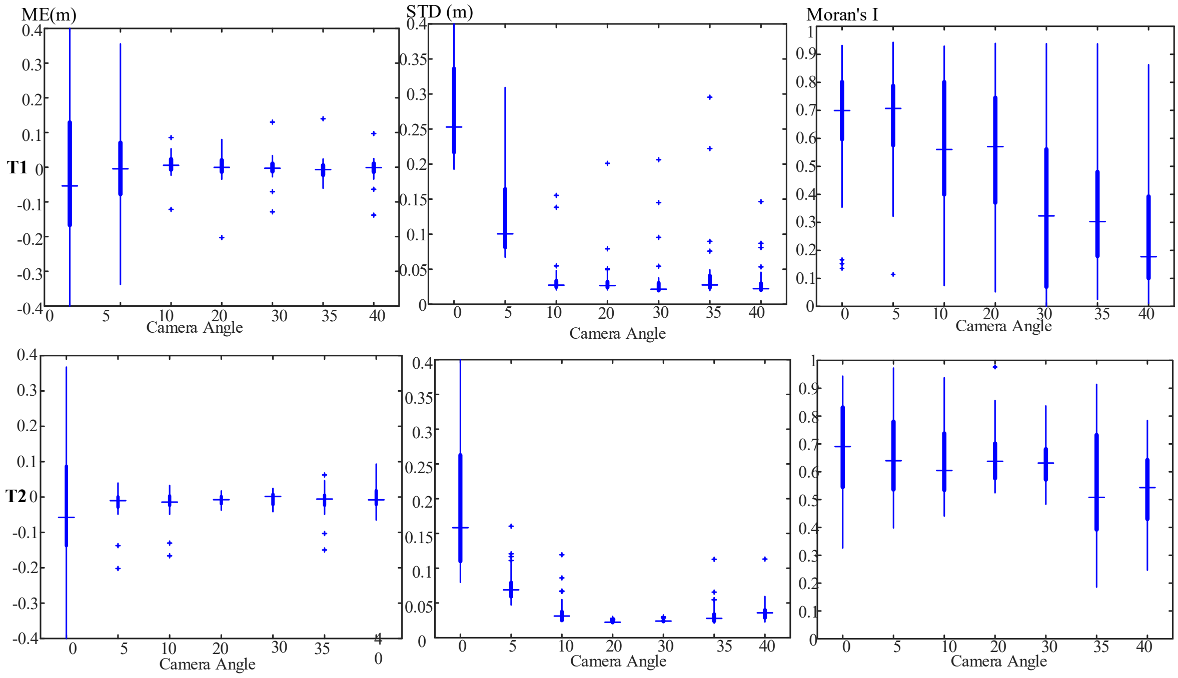

Figure 4. The ME and STD against camera angle in scenario of control-free

Besides the ME and STD, it is important to look at the spatial distribution of errors (Eltner et al., 2016; James et al., 2020; Smith and Vericat, 2015). Fig. 5 shows an example of the spatial distribution of GCP errors. When the images are captured with a nadir camera inclination, the distribution of error appears spatially-structured at both sites, which suggests the presence of some systematic distortions (e.g., 'doming'). For example, in T1 area, many negative errors were located on the ridges in the northeast and southwest, whilst positive errors located on the gully bottom (Fig.5). The Moran's I values trend towards zero as camera angle increases (Fig.4). This result indicates that the spatial correlation of errors is reduced with higher camera angles (especially greater than 20°). Thus, the use of an inclined camera is likely to have improved calibration and so reduced the degree of spatially-dependent systematic error.

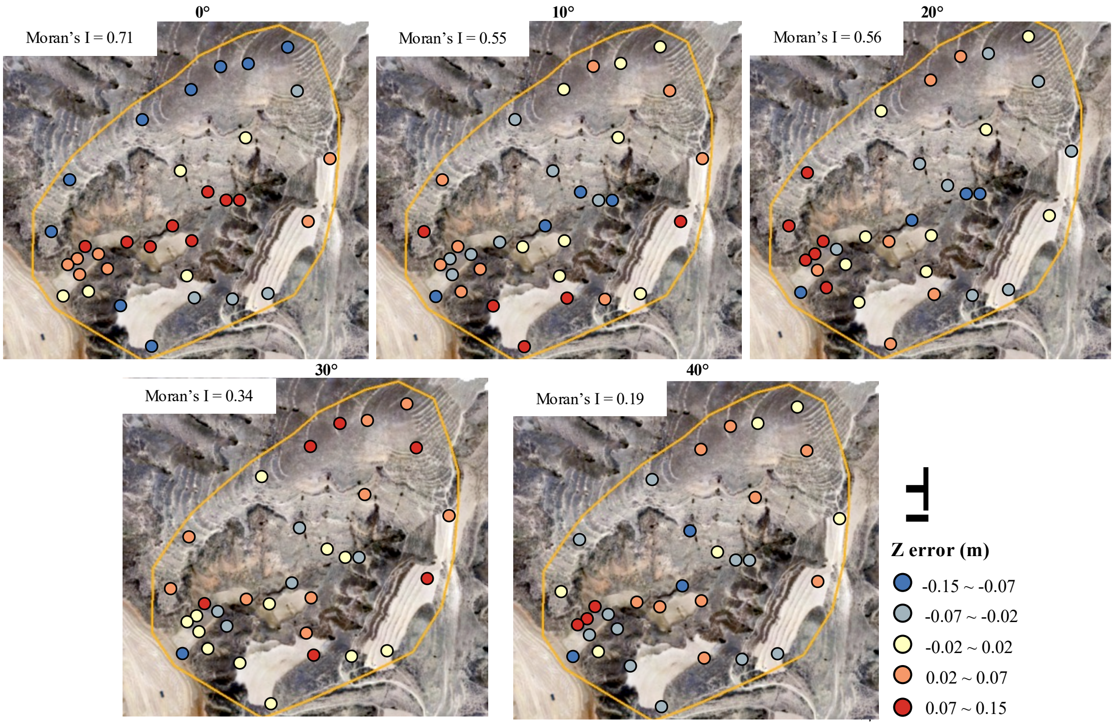

Figure 5. The spatial distribution of GCP errors under different camera angle in the T1 area

To understand further these results, we investigated the correlations between camera parameters for different camera angles (Fig.6). Correlation between radial distortion parameters (*K1, K2, K3*) is expected. Similarly, correlations between focal length (*f*) and principal point offset (*Cx, Cy*), and (*Cx, Cy*) and tangential distortion parameters (*P1, P2*) are also common. Work has shown (James et al., 2020) that correlation between radial distortion parameters and principal point offset and tangential distortion parameters (marked by the red dashed ellipse in the Fig. 6) is indicative of calibrations with a higher probability of causing systematic error in derived data. For the camera angles of 0 and 5 °, the correlations are strong (Fig. 6). With increasing camera angle, the correlations decrease to low levels by 20°. This result suggests that higher camera angle enhanced the camera calibration.

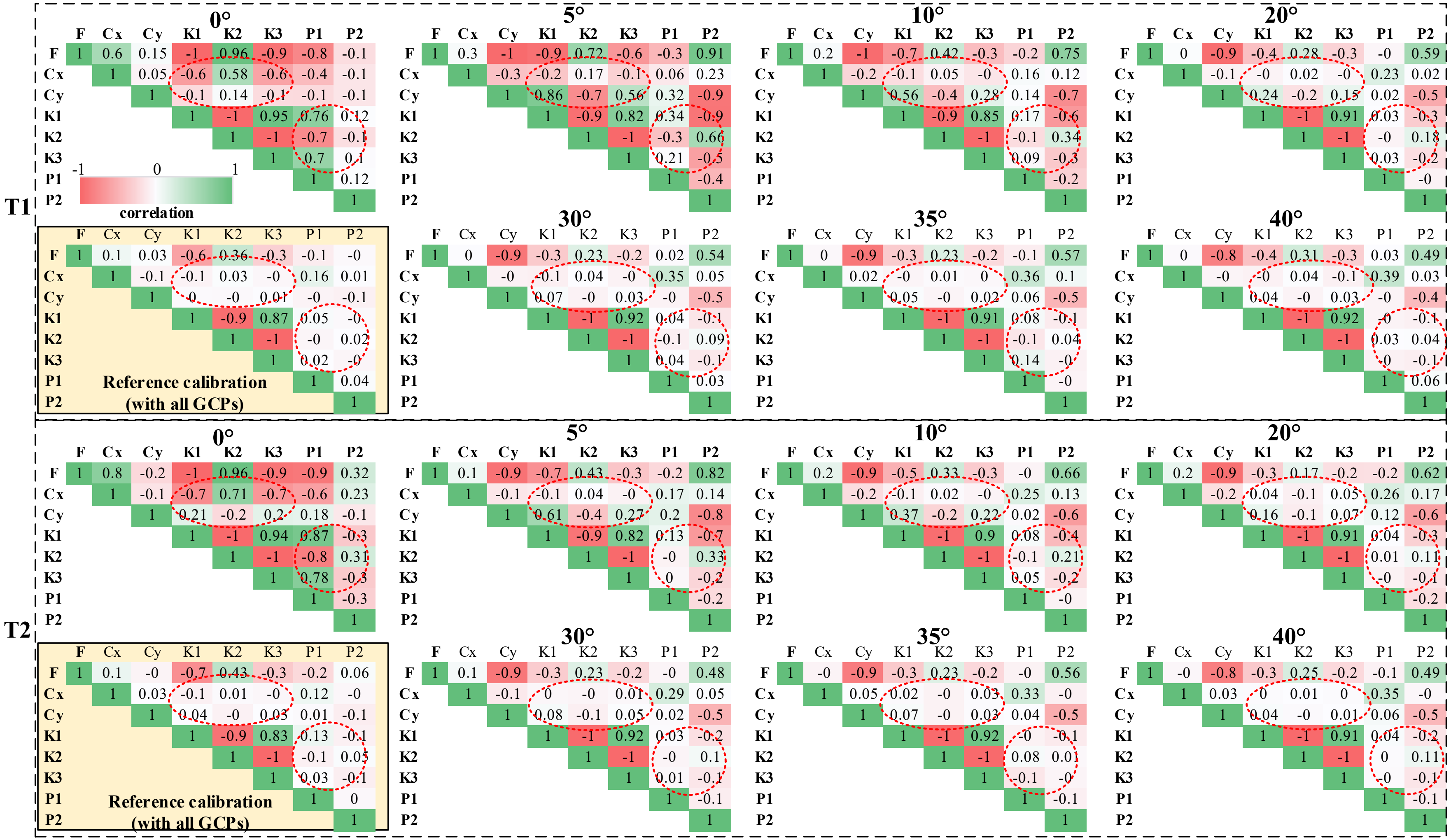

Figure 6. Correlations of camera parameters with different camera angle (The box with yellow back ground is the correlations of reference calibration.)

3.1.2 Interactions between camera angle and GCPs

The results of the Monte Carlo experiments considering GCP quantity and distribution are presented in Fig. 7. The median of ME and STD of check points declines with the number of GCPs at first and then becomes stable close to ~0 m and ~0.02 m, respectively. Adding a relatively small number of GCPs quickly improves the accuracy (from ~0.5 m to ~0 m) and precision (from ~±0.25 m to ~±0.02 m). Further increases in the number of GCPs have only a minor effect on error. However, when the number of GCPs is very large (i.e. 30 – 31 in the T1 area and 28 – 29 in the T2 area), the ME and STD slightly increase to ~ ±0.01 m and 0.03 m, respectively (Fig. 7), because the small number of check points increases the uncertainty in the validation data, that is estimates of ME and STD.

Fig. 7 also shows the effect of camera inclination angle on the optimal number of GCPs. On the one hand, higher camera inclination clearly reduces ME and STD when there are no or only a few (< 5) of GCPs (Fig. 7); but, once GCPs are more than ~5, the camera inclination angle seems to have little effect on ME and STD. On the other hand, high camera inclination appears to reduce the number of GCPs needed to obtain the same accuracy (Fig. 7). For example, the ME and STD with 3 GCPs is ~0 and ~0.05 m, respectively, with the 20 – 40° camera inclination scenarios; but it needs 6 – 7 GCPs for the 0 – 5° camera inclination scenarios.

The changes in the ranges of boxes in Fig. 7 implies an effect of GCP distribution (or selection of GCPs). The box ranges decrease with the number of GCPs, which suggests the distribution of GCPs is crucial when the number of GCPs is small (≤ 5), but becomes less important with increasing number of GCPs (> 5). This may be because the probability of better distributed GCPs increases with number of GCPs. On the other hand, although the box ranges are relatively high with a small number of GCPs, high camera inclination is beneficial to reduce the variability (box range in Fig. 7).

To better reveal the structure of errors, Figure 7 shows the Moran's I of different scenarios. Note that we did not calculate the Moran's I when the number of GCPs was more than 25, because the number of remaining check points became too small for Moran's I calculation. The Moran's I tended towards 0 with an increasing number of GCPs (from 2 to 25). Addition of GCPs is thus beneficial for improving the structure of errors. With fewer GCPs (≤ 5), the Moran's I declined with camera angle, but this effect became less clear with an increasing number of GCPs (> 5). Although the ME and STD are stable when GCP number is more than 5, Moran’s I can be further improved with more GCPs. Thus, increasing the number of GCPs beyond that suggested by the ME and STD is necessary to eliminate the spatial dependence of errors.

37

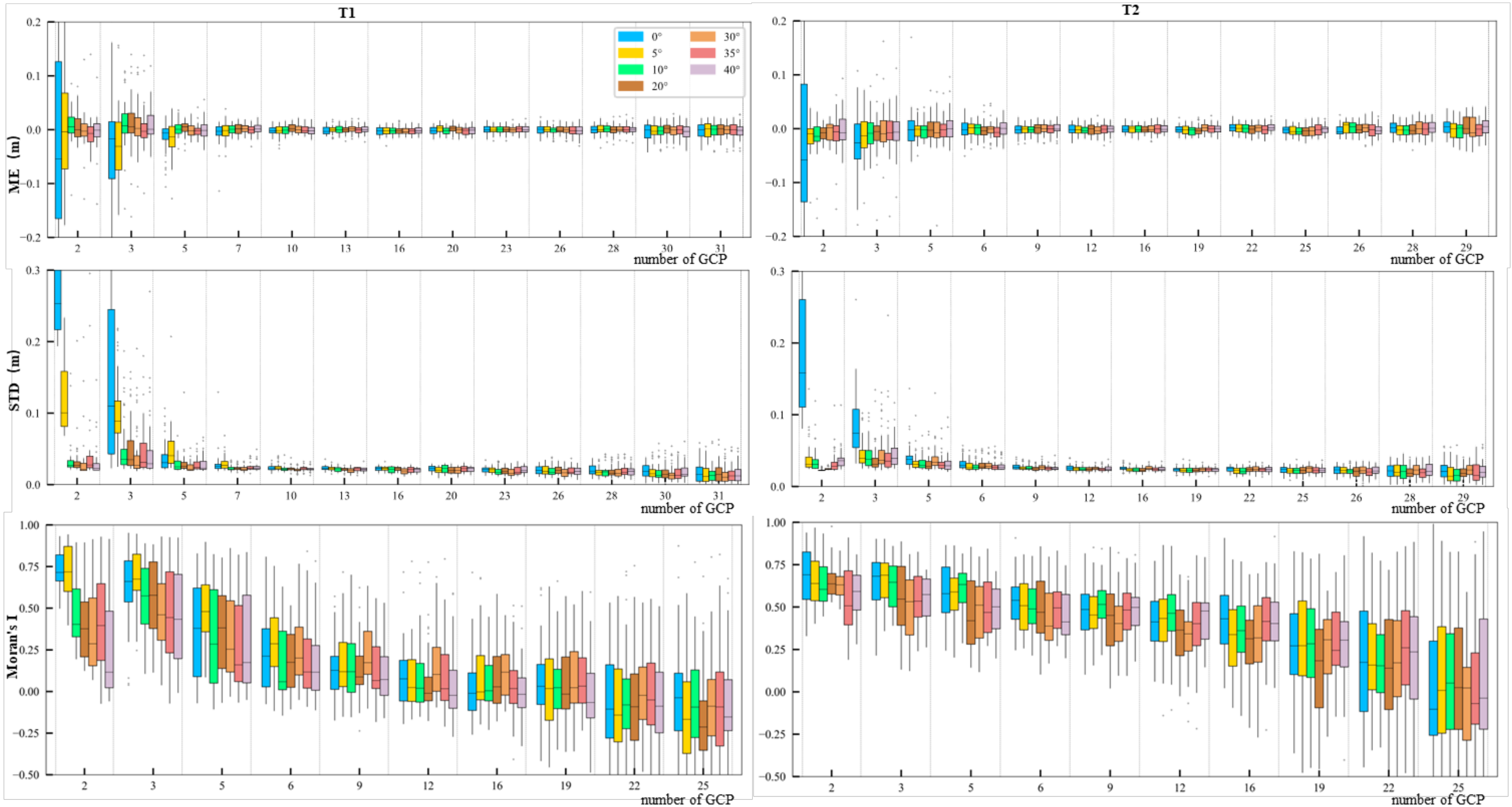

38 Figure 7. The results of Monte Carlo GCP test with different camera angle

3.2 Impacts of flying height

3.2.1 Impacts of flying height without GCPs

The sensitivity of precision and accuracy to flying height is relative to the camera angle in the control-free scenario (Fig. 8). We used a nadir (0°) camera in the T1 area and find increasing ME and STD values with increasing flight height (Fig.8). Meanwhile, the ME and STD are relatively stable in the T2 area where a 15° camera angle was used. Thus, oblique photography reduces the sensitivity of ME and STD to flying height. However, the Moran's I values have an increasing trend with flying height, and this effect is not affected by camera angle (same trend in T1 and T2 area).

Generally, the ME and STD would increase with flying height due to an increase of observation distance and coarser image resolution. The T2 area shows an unexpected result. This could be due to two reasons. First, in this study, the vertical measurement precision of the RTK survey of the GCPs was about ±2 cm. The measurement precision would be not enough to capture the changes of ME and STD in T2 area because the oblique photography reduced the ME and STD. Second, this result could mean that the photogrammetric solutions were still dominated by camera calibration effects, not flying height.

Fig. 8 also supports previous observations (Fig. 4, 6, 7) that the accuracy of results using oblique photography is higher than that of vertical photography. The ME and STD are always around decimeters in T1 area (nadir photography); whereas, with the oblique photography, they all are around centimeters in T2.

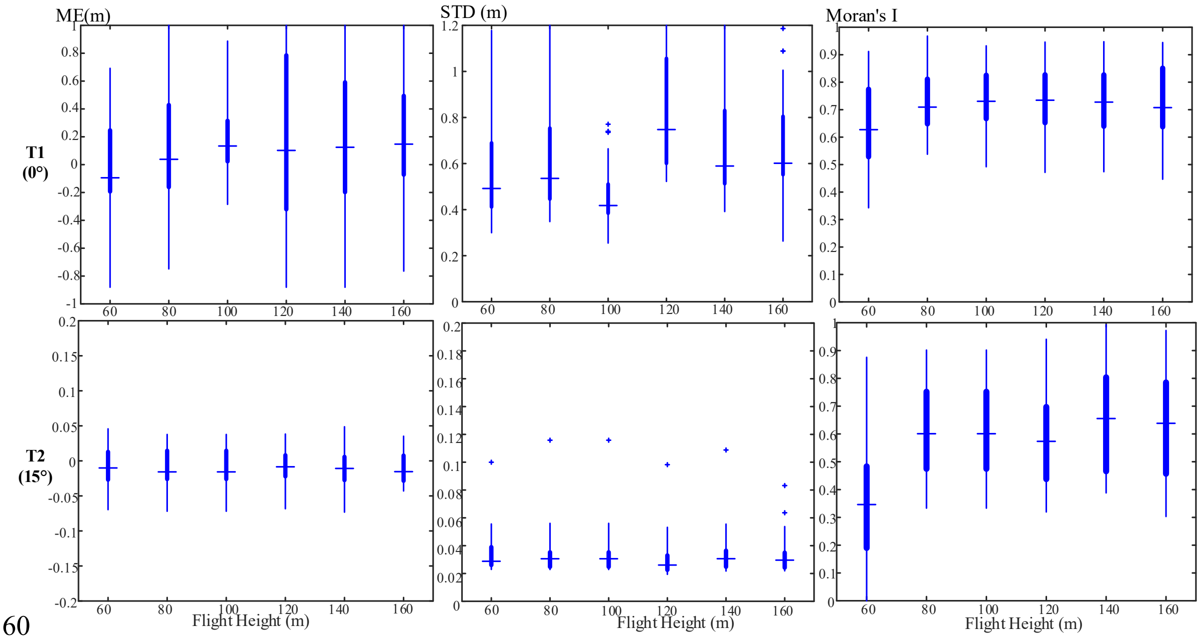

Figure 8. The ME and STD against flight height

3.2.2 Interactions between flying height and GCPs

The Monte Carlo GCP experiment was carried out with images captured at different flying heights. As observed earlier, the addition of a small number of GCPs quickly improves the accuracy and precision, but further increases in the number of GCPs has only minor effect, which is also supported by Fig. 9. With a small number of GCPs (2 – 3 GCPs), the ME increases with flying height for T1; while, the changes for T2 were not obvious due to the use of oblique photography. With more GCPs, the flying height had a minor effect on ME. However, with 5 – 19 GCPs, the variability (box range) in STD decreased with flying height in the two areas. This means that with low flying height (high ground resolution), the selection of GCPs becomes important. Fig. 9 also shows that the optimal GCP number is not sensitive to the flying height. Although the flight height changes from 60m to 160m, the GCP optimal number in the T1 area (0° camera) is always about 7 and that of the T2 area (15° camera) is always about 9.

With a small number of GCPs, the Moran's I increases with flying height. However, the flying height had only a minor effect on the Moran's I when more GCPs were used. Fig. 9 also confirmed that the Moran's I can be further improved with more GCPs after the ME and STD have stabilised. Note that the variability (box range in Figure 9) of Moran's I increases with the number of GCPs. This is because the decreasing number of check points would lead to uncertainty in calculating Moran's I.

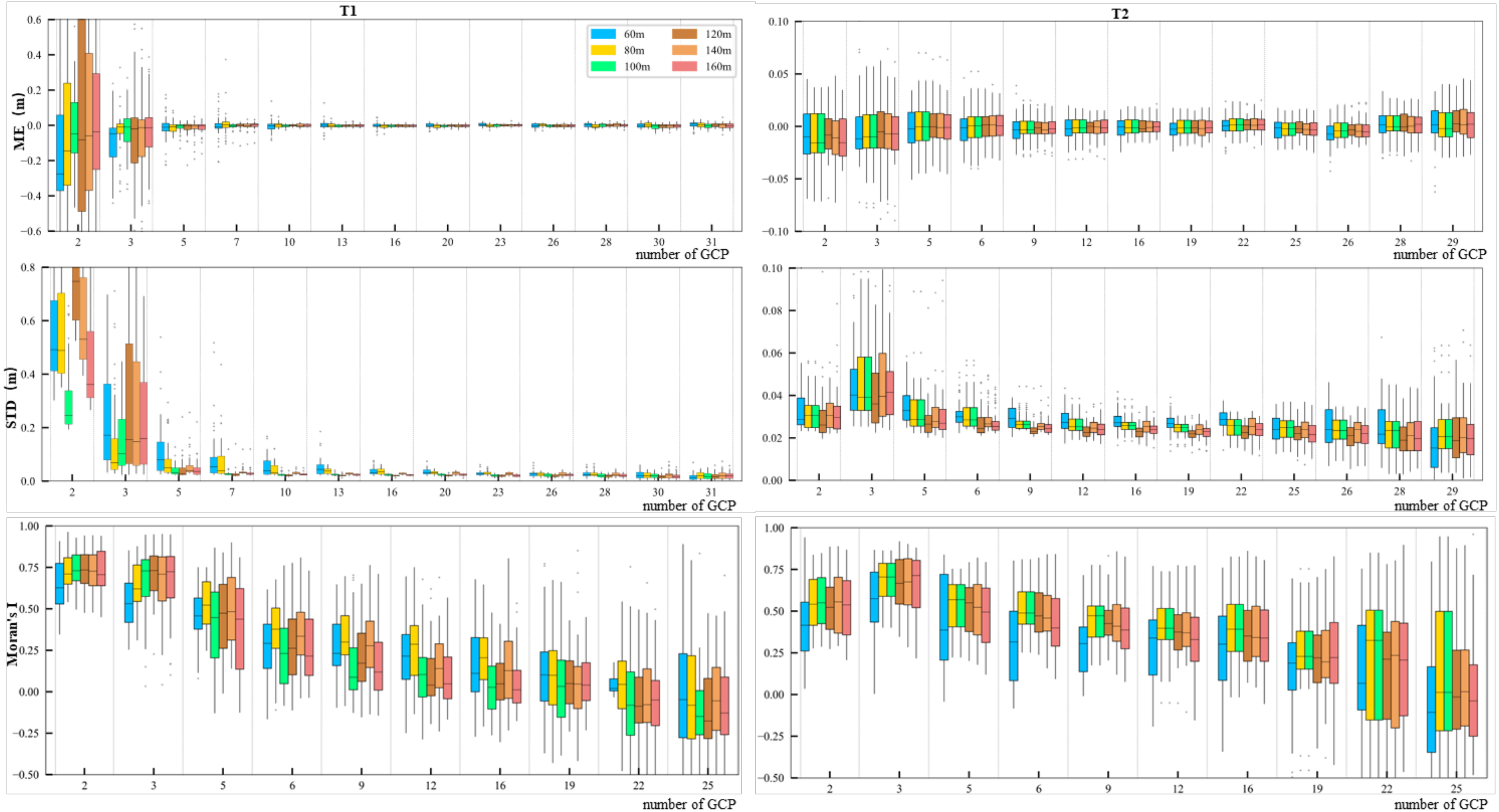

Figure 9. The results of Monte Carlo GCP test with different flying heigh

3.3 Effects of combination datasets

3.3.1 Effects of combination datasets without GCPs

Fig. 10 shows the ME, STD, and Moran's I for different combinations of camera angle for the GCP-unconstrained scenario. The ME is low and stable for each main block and only marginally changes with the angle of added images. The STD and Moran's I changes more obviously than ME. With main block angles of 0 to 5°, the STD and Moran's I decrease with progressively higher angles of added images (especially if the angle of supplemented images is greater than 20°). However, if the main block angle is greater than 10°, adding imagery with greater angles has negligible effect on the STD and Moran's I. Thus, higher angle of supplemented imagery is necessary for situations where most imagery is nadir or close to nadir but not otherwise.

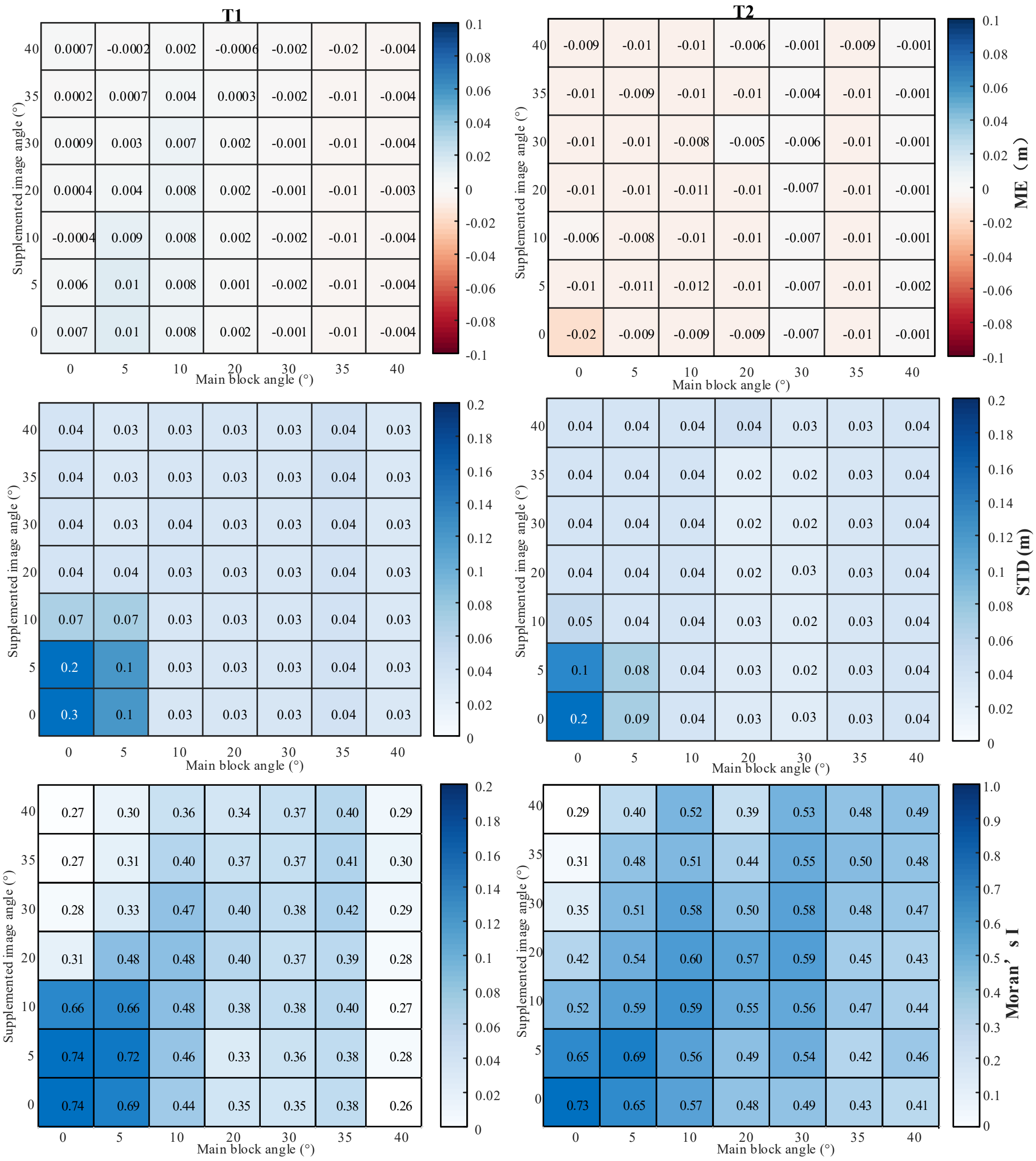

Figure 10. The ME and STD of different combinations of main blocks and supplemented images.

Fig. 11 shows the ME, STD, and Moran’s I with different combination of flying heights. The combined multiple flying height has no effect on ME and Moran’s I, but does affect the STD. In the T1 area, the STD shows a decreasing trend when the number of flying heights increases from one to two. Flying height seems to have no effect on STD in area T2. The difference between T1 and T2 may be because in T2, with all flights conducted with a 15° inclined camera, the within-image observation distances are variable, such that adding different flying heights has no clearly distinguishable effect with off-nadir imagery.

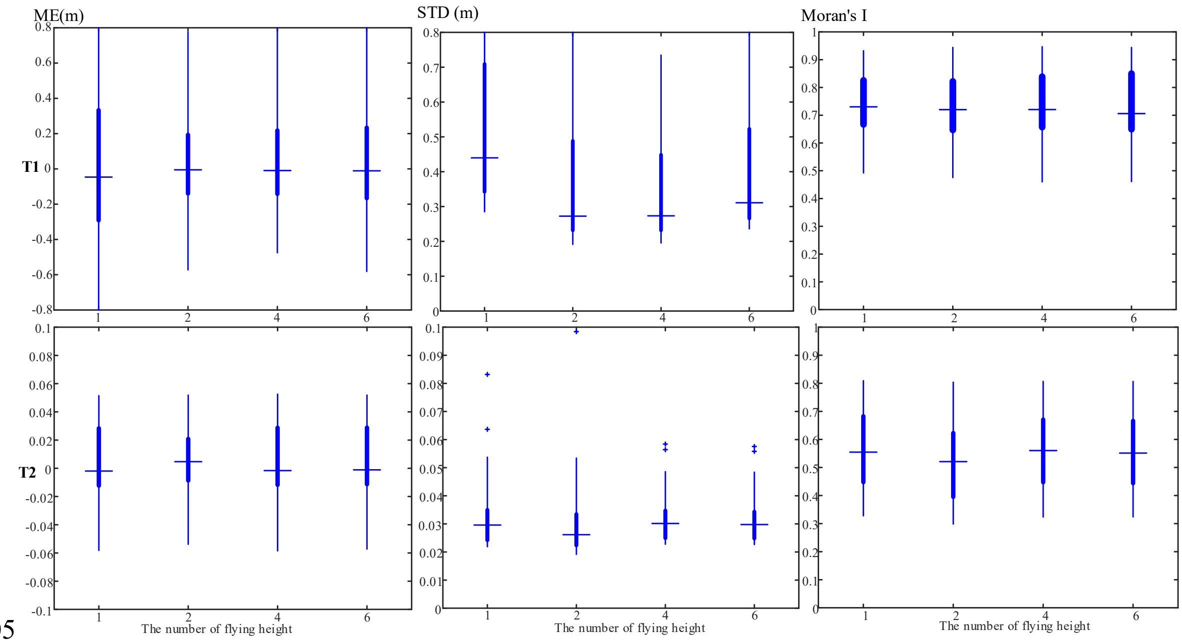

Figure 11. The effect of multiple flying height combination on ME and STD.

3.2.2 Interactions between combination datasets and GCPs

The Monte Carlo GCP experiment was implemented for different combinations of main blocks and added images. The effect of GCP quantity on ME and STD for each combination is similar to Fig. 7: the errors decline with the number of GCPs at first and then become stable. Here, we mainly focus on whether the combinations of main blocks and added images affect the optimal GCP number. Starting with initial angles of 0 – 5°, the optimal number declines marginally with addition of higher angle imagery (Fig. 12). Moreover, there are no obvious changes in the optimal GCP number when the initial angles are greater than 10. Thus, whilst combining higher angle imagery with low angle imagery may improve precision and accuracy (Fig. 10), the number of required GCPs is insensitive to whether high angle imagery is added or not.

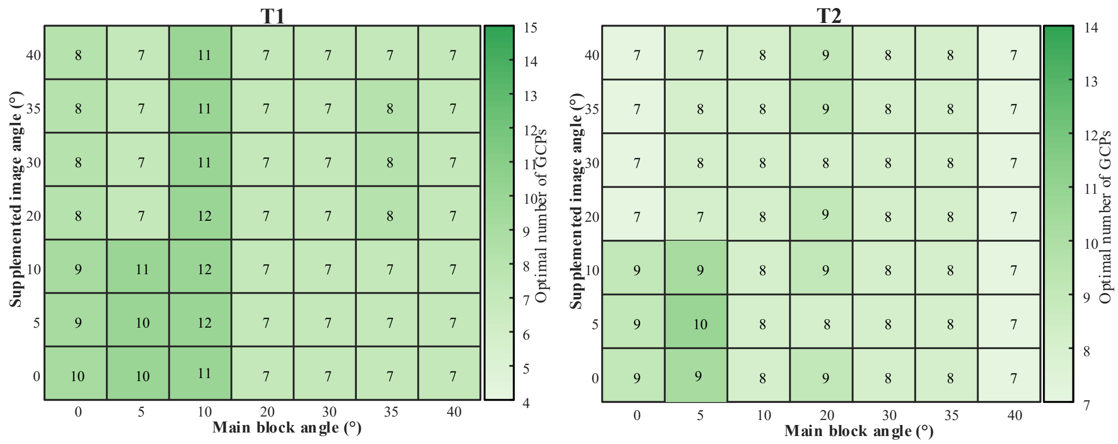

Figure 12. The GCP optimal number in different combinations of main blocks and supplemented images.

Fig. 13 shows the Monte Carlo GCP experiment with different combinations of flying heights. The ME, STD, and Moran's I have similar patterns to Fig 7 and 9: ME and STD decrease with addition of a small number of GCPs and then become stable, whilst Moran's I can further decrease with number of GCPs.

For the same number of GCPs, the number of combined flying heights seems to have no effect on ME and Moran's I; whilst, for T1 only, the greater the combined number of flying heights, the lower the STD at 5 to 20 GCPs. This is consistent with Fig. 11, which means that combinations of multiple flight heights (observation distances) are beneficial for reducing errors with imagery at nadir, but this seems unnecessary in the scenario with a highly inclination camera. Even a small number of GCPs, 5 or more, substantially reduces STD and has much more effect than addition of flying heights. Indeed, with a larger number of GCPs, the optimal precision and accuracy are not higher than blocks with only one flight height (Fig. 9 and 13).

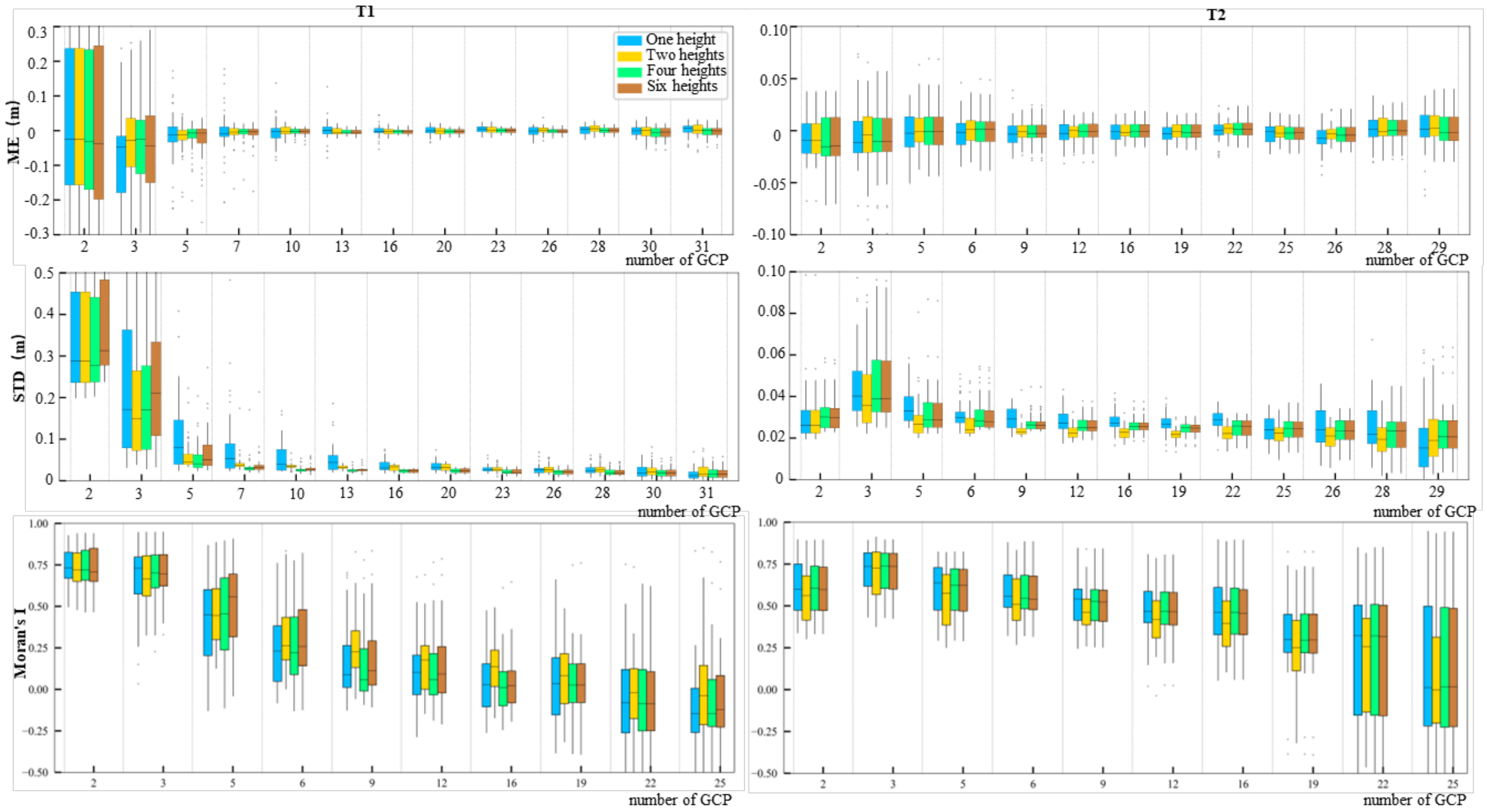

Figure 13. The results of Monte Carlo GCP test with different combinations of flying heights

4 Discussion

4.1 Image collection strategies

Systematic errors such as ‘doming’ and ‘dishing’ in nadir image blocks and small off-nadir blocks have now been frequently described in applications of SfM-MVS photogrammetry using UAVs (Carbonneau and Dietrich, 2017; James et al., 2020; Nesbit and Hugenholtz, 2019). Oblique photography and combined dataset strategies have been proposed for addressing this challenge by seeking more robust camera calibrations (James and Robson, 2014; Nesbit and Hugenholtz, 2019; Rossi et al., 2017; Wackrow and Chandler, 2011). Our results confirm the improvement of derived DEM accuracy and precision of SfM-MVS derived point clouds when oblique imagery is used. However, this study also provides further insights into optimal image collection strategies.

A high camera inclination not only decreases the magnitude of errors (Fig. 4), but also mitigates its spatial correlation (Moran’s I) (Fig. 5) and hence the degree of doming/dishing. It enhances camera calibration by reducing unwanted correlation between radial and decentering distortion parameters of the camera model (Fig. 6). This improvement may be related to the fact that the increasing intersection angles of rays of tie points enhances the bundle adjustment, and then improves camera calibration and mitigates errors. Additionally, steep slopes, which are not easily visible in nadir images, may be better captured by oblique images (Petrie, 2009), resulting in more potential matching points during the bundle adjustment. This result is consistent with findings of Vacca et al. (2017), who reported that oblique images enhanced tie point matching. Notably, James et al. (2020) reported that a small inclination angle could increase systematic errors and suggested that we should move beyond ‘off-nadir’ imagery. We also found that the use of small inclination angle needs more GCPs in the T1 area (Fig. 12); but this effect does not appear in the T2 area, which means that this effect could be relative to other factors (such as topographic characteristics, image quality, and camera properties). Nevertheless, a small inclination angle is not recommended in UAV-SfM practice.

Generally, the precision and accuracy decrease with flying height. Scholars (Smith and Vericat, 2015) used the precision ratio between precision and average observation distance to quantifying the effect of flying height. In this study, the results show that the effect of flying height is relative to the camera angle (Fig. 8). The precision ratio increased from 1:800 to 1:2000 with high camera inclination. This finding is important because it means that with the same requirement of precision, the flying height in field work can be relatively higher by using oblique photography thus improving workflow efficiency. However, notably, the spatial correlation of error (Moran's I) increases with flying height if GCP-free (Fig. 8). Thus, need for GCPs increases as the flying height increases.

A nadir image block supplemented with convergent images and combinations of multiple flying height were suggested for improving UAV-SfM calibrations in previous studies (James and Robson, 2014; Nesbit and Hugenholtz, 2019). A high camera inclination block supplemented with convergent images and combined multiple flying height blocks were first investigated in this study (Fig. 10). Our results show that such additional data may not be necessary if there is imagery with a high inclination. With inclined imagery, the need for multiple flying heights was reduced which we attributed to the effects of off-nadir imagery on the range of image to object distances present in anyone scene.

4.2 Ground control quantity

Image collection strategies are crucial when surveys are GCP-free or only a small number of GCPs is used, but become less important with more GCPs (Fig. 7, 9, and 13). GCPs provide constraints for the bundle adjustment and define absolute position and orientation to SfM-derived point clouds (James and Robson, 2014; James et al., 2017a; Rupnik et al., 2015), which substantially improve model accuracy and precision. Our results show that the ME and STD of check points decline quickly with a small number of GCPs in all scenarios (Fig. 7 and 9), but a large number of GCPs are unnecessary. This finding is similar to Stöcker et al (2020). However, we also found that the effects of GCP quantity interact with image collection strategies.

High camera inclination seems to reduce requirements for GCPs (Fig 7). This may be related to the terrain characteristics at each site. We selected the study areas (T1 and T2) in high-relief terrain. Oblique images with higher inclination angle are expected to capture steep slopes and match more tie points (Vacca et al., 2017). Due to more tie points and more uniform spatial resolution (or point density) in oblique photography (Petrie, 2009), the aerial triangulation should be enhanced, so reducing dependency on GCPs.

The flying height and combination dataset strategies had little effect on the number of GCPs needed. In most of the scenarios we studied, 5 to 9 GCPs (1.39 to 1.76 GCP/ha) were enough to improve the bundle adjustment. The suitable GCP number could be related to the area of study sites. In this study, the study area is small (3.6 – 5.1 ha) which requires fewer GCPs. However, Cabo et al. (2021) reported that 50 GCPs were necessary for a 1220 ha study area (0.041 GCP/ha). Thus, the average GCP density is more useful than optimal GCP number in practice. The average required GCP density appears to vary between studies (Cucchiaro et al., 2018; Dai et al., 2022; James et al., 2020; Stöcker et al., 2020), which means that it is still relative to other factors, such as terrain relief, surface texture, and image quality. Hence, with the exception of the effect of image collection strategies, there is no uniform recommendation for average GCP density or optimal number of GCPs in different areas.

Although the magnitude of errors (ME and STD) stabilizes rapidly with increasing GCPs, the structure of errors (Moran's I) can be further improved with more GCPs (Fig. 7, 9, and 13). The addition of GCPs is necessary for improving the structure of errors. In this study, the median of Moran's I is close to 0 with more than 22 GCPs (Fig. 7, 9, and 13); it only needs 5-9 GCPs for ME and STD stable. Moreover, the camera angle, flying height, and combination dataset strategies have only minor effects on the necessary GCP numbers for Moran's I to stabilize.

Besides the number of GCPs, the spatial distribution of GCPs should be addressed (Cabo et al., 2021; James et al., 2017a). Our study showed that, with the fixed number of GCPs, the different selections of GCPs have different ME, STD, and Moran's I (Fig.7, 9, and 13). Studies proposed that a combination of edge distribution and stratified distribution is the best practice for GCPs (Martínez-Carricondo et al., 2018b). Our study argues that the effect of GCP distribution is less important than the number of GCPs in small study areas, which is supported by the reduction of error variability in Fig.7 and Fig. 9. This may be because the probability of better distributed CGPs increases with number of GCPs. However, the small size of the study areas may prevent the effects of spatial distribution of GCPs being thoroughly assessed and that the spatial distribution is likely to be more important over larger areas.

Finally, the image collection and ground control strategies are not only applicable for high-relief areas, but also low-relief regions. The oblique photography is also beneficial for improving terrain modeling accuracy in low-relief regions (e.g., Carbonneau and Dietrich, 2017; James et al., 2020). However, the terrain relief seems to be another variable that influence UAV-SfM photogrammetry accuracy. The UAV-SfM terrain modeling errors in low-relief regions is less complex than that of high-relief regions (James et al., 2020), which could reduce the requirement of GCPs.

5 Conclusion

This study designed various photogrammetric scenarios and investigated the effects of image collection strategies, ground control quantity, and their interaction on terrain modelling errors (ME and STD) and their spatial structure (Moran's I) in high-relief terrain. The latter is an important addition to the error metrics that should be used in assessing SfM-MVS results. The work showed clearly that standard error statistics like ME and STD may be found to be acceptable even when spatial structure in the error field remains, something that is revealed with Moran's I. The latter should be routinely applied in evaluations of the quality of UAV SfM-MVS results.

The results provide insights for improving UAV SfM-MVS practices. First, a high camera inclination (20°-40°) enhances camera calibration by reducing unwanted correlation between radial and decentering distortion parameters of the camera model. This not only decreases the magnitude of errors, but also mitigates its spatial correlation (Moran's I). Second, a high flying height increases ME, STD, and Moran's I. However, the effect of flying height interacts with camera angle. Oblique photography reduces the sensitivity of ME and STD to flying height, but not for Moran's I. Third, the supplemented datasets (a main block supplemented with convergent images and combined multiple flying height blocks) is not necessary if there is imagery with a high inclination.

GCPs provide more substantial constraints for bundle adjustment than image collection strategies. On the one hand, the magnitude of errors (ME and STD) declines quickly with a small number of GCPs and then become stable in all scenarios, but the structure of errors (Moran's I) can be further improved with increasing GCPs. This means that the structure of errors (such as "doming") needs more attention in UAV-SfM practice. On the other hand, the effects of GCP quantity interact with image collection strategies. High camera inclination seems to reduce requirements for GCPs, while the flying height and combination dataset strategies have little effect on necessary GCP quantity. Moreover, the distribution of GCPs still affects the errors, but the effect of GCP distribution becomes less important with the increase in the number of GCPs.

Reference

Adams, S.M., Levitan, M.L., Friedland, C.J., 2014. High resolution imagery collection for post-disaster studies utilizing unmanned aircraft systems (UAS). Photogrammetric Engineering & Remote Sensing, 80, 1161-1168.

Agueera-Vega, F. et al., 2018. Reconstruction of extreme topography from UAV structure from motion photogrammetry. Measurement, 121, 127-138.

Bakker, M. and Lane, S.N., 2017. Archival photogrammetric analysis of river-floodplain systems using Structure from Motion (SfM) methods. Earth Surface Processes and Landforms, 42, 1274-86

Cabo, C., Sanz-Ablanedo, E., Roca-Pardinas, J., Ordonez, C., 2021. Influence of the Number and Spatial Distribution of Ground Control Points in the Accuracy of UAV-SfM DEMs: An Approach Based on Generalized Additive Models. IEEE Transactions on Geoscience and Remote Sensing, 59, 10618-10627.

Carbonneau, P.E., Dietrich, J.T., 2017. Cost-effective non-metric photogrammetry from consumer-grade sUAS: implications for direct georeferencing of structure from motion photogrammetry. Earth Surface Processes and Landforms, 42, 473-486.

Carvajal-Ramírez, F., Agüera-Vega, F., Martínez-Carricondo, P.J., 2016. Effects of image orientation and ground control points distribution on unmanned aerial vehicle photogrammetry projects on a road cut slope. Journal of Applied Remote Sensing, 10, 034004.

Cucchiaro, S. et al., 2018. Monitoring topographic changes through 4D-structure-from-motion photogrammetry: application to a debris-flow channel. Environmental Earth Sciences, 77.

Dai, W. et al., 2022. Monitoring and modeling sediment transport in space in small loess catchments using UAV-SfM photogrammetry. Catena, 214, 106244.

Dai, W. et al., 2019. Effects of DEM resolution on the accuracy of gully maps in loess hilly areas. Catena, 177, 114-125.

Eltner, A., Baumgart, P., Maas, H.G., Faust, D., 2015. Multi‐temporal UAV data for automatic measurement of rill and interrill erosion on loess soil. Earth Surface Processes and Landforms, 40, 741-755.

Eltner, A. et al., 2016. Image-based surface reconstruction in geomorphometry–merits, limits and developments. Earth Surface Dynamics, 4, 359-389.

Escobar Villanueva, J.R., Iglesias Martínez, L., Pérez Montiel, J.I., 2019. DEM generation from fixed-wing UAV imaging and LiDAR-derived ground control points for flood estimations. Sensors, 19, 3205.

Harwin, S., Lucieer, A., 2012. Assessing the accuracy of georeferenced point clouds produced via multi-view stereopsis from unmanned aerial vehicle (UAV) imagery. Remote Sensing, 4, 1573-1599.

Harwin, S., Lucieer, A., Osborn, J., 2015. The impact of the calibration method on the accuracy of point clouds derived using unmanned aerial vehicle multi-view stereopsis. Remote Sensing, 7, 11933-11953.

Hugenholtz, C.H. et al., 2013. Geomorphological mapping with a small unmanned aircraft system (sUAS): Feature detection and accuracy assessment of a photogrammetrically-derived digital terrain model. Geomorphology, 194, 16-24.

James, M.R., Antoniazza, G., Robson, S., Lane, S.N., 2020. Mitigating systematic error in topographic models for geomorphic change detection: accuracy, precision and considerations beyond off‐nadir imagery. Earth Surface Processes and Landforms.

James, M.R. et al., 2019. Guidelines on the use of structure‐from‐motion photogrammetry in geomorphic research. Earth Surface Processes and Landforms, 44, 2081-2084.

James, M.R., Robson, S., 2014. Mitigating systematic error in topographic models derived from UAV and ground-based image networks. Earth Surface Processes and Landforms, 39, 1413-1420.

James, M.R., Robson, S., d'Oleire-Oltmanns, S., Niethammer, U., 2017a. Optimising UAV topographic surveys processed with structure-from-motion: Ground control quality, quantity and bundle adjustment. Geomorphology, 280, 51-66.

James, M.R., Robson, S., Smith, M.W., 2017b. 3-D uncertainty-based topographic change detection with structure-from-motion photogrammetry: precision maps for ground control and directly georeferenced surveys. Earth Surface Processes and Landforms, 42, 1769-1788.

Jiang, S., Jiang, W., Huang, W., Yang, L., 2017. UAV-based oblique photogrammetry for outdoor data acquisition and offsite visual inspection of transmission line. Remote Sensing, 9, 278.

Lane, S.N., Gentile, A., Goldenschue, L., 2020. Combining UAV-based SfM-MVS photogrammetry with conventional monitoring to set environmental flows: modifying dam flushing flows to improve alpine stream habitat. Remote Sensing, 12, 3868.

Martínez-Carricondo, P. et al., 2018a. Assessment of UAV-photogrammetric mapping accuracy based on variation of ground control points. International journal of applied earth observation and geoinformation, 72, 1-10.

Martínez-Carricondo, P., Mesas-Carrascosa, F.J., García-Ferrer, A., güera-Vega, F.A., Pérez-Porras, F., 2018b. Assessment of UAV-photogrammetric mapping accuracy based on variation of ground control points. International Journal of Applied Earth Observation & Geoinformation, 72, 1-10.

Meinen, B.U., Robinson, D.T., 2020. Mapping erosion and deposition in an agricultural landscape: Optimization of UAV image acquisition schemes for SfM-MVS. Remote Sensing of Environment, 239, 111666.

Moran, P.A., 1950. Notes on continuous stochastic phenomena. Biometrika, 37, 17-23.

Nesbit, P., Hugenholtz, C., 2019. Enhancing UAV–SfM 3D Model Accuracy in High-Relief Landscapes by Incorporating Oblique Images. Remote Sensing, 11, 239.

Nieminski, N.M., Graham, S.A., 2017. Modeling stratigraphic architecture using small unmanned aerial vehicles and photogrammetry: examples from the Miocene East Coast Basin, New Zealand. Journal of Sedimentary Research, 87, 126-132.

Ouedraogo, M.M., Degre, A., Debouche, C., Lisein, J., 2014. The evaluation of unmanned aerial system-based photogrammetry and terrestrial laser scanning to generate DEMs of agricultural watersheds. Geomorphology, 214, 339-355.

Padró, J.-C., Muñoz, F.-J., Planas, J., Pons, X., 2019. Comparison of four UAV georeferencing methods for environmental monitoring purposes focusing on the combined use with airborne and satellite remote sensing platforms. International journal of applied earth observation and geoinformation, 75, 130-140.

Petrie, G., 2009. Systematic Oblique Aerial Photography Using Multiple Digital Cameras Oblique Photography -Introduction I -Multiple Oblique Photographs. Photogrammetric Engineering & Remote Sensing, 75, 102-107.

Polat, N., Uysal, M., 2018. An experimental analysis of digital elevation models generated with Lidar Data and UAV photogrammetry. Journal of the Indian Society of Remote Sensing, 46, 1135-1142.

Rangel, J.M.G., Gonçalves, G.R., Pérez, J.A., 2018. The impact of number and spatial distribution of

GCPs on the positional accuracy of geospatial products derived from low-cost UASs. International journal of remote sensing, 39, 7154-7171.

Roncoroni, M. et al., 2022. Centimeter-scale mapping of phototrophic biofilms in glacial forefields using visible band ratios and UAV imagery. International Journal of Remote Sensing, 1-35.

Roncoroni, M., Mancini, D., Miesen, F., Müller, T., Gianini, M., Ouvry, B., Clémençon, M., Lardet, F., Battin, T.J. and Lane, S.N., 2023. Decrypting the stream periphyton physical habitat of recently deglaciated floodplains. Science of the Total Environment, 867, Article number 161374

Rossi, P., Mancini, F., Dubbini, M., Mazzone, F., Capra, A., 2017. Combining nadir and oblique UAV imagery to reconstruct quarry topography: methodology and feasibility analysis. European Journal of Remote Sensing, 50, 211-221.

Rupnik, E., Nex, F., Toschi, I., Remondino, F., 2015. Aerial multi-camera systems: Accuracy and block triangulation issues. ISPRS Journal of Photogrammetry and Remote Sensing, 101, 233-246.

Sanz‐Ablanedo, E., Chandler, J.H., Ballesteros‐Pérez, P., Rodríguez‐Pérez, J.R., 2020. Reducing systematic dome errors in digital elevation models through better UAV flight design. Earth Surface Processes and Landforms, 45, 2134-2147.

Smith, M.W., Vericat, D., 2015. From experimental plots to experimental landscapes: topography, erosion and deposition in sub‐humid badlands from Structure‐from‐Motion photogrammetry. Earth Surface Processes and Landforms, 40, 1656-1671.

Stöcker, C., Nex, F., Koeva, M., Gerke, M., 2020. High-quality uav-based orthophotos for cadastral mapping: Guidance for optimal flight configurations. Remote sensing, 12, 3625.

Stott, E., Williams, R.D., Hoey, T.B., 2020. Ground control point distribution for accurate kilometre-scale topographic mapping using an RTK-GNSS unmanned aerial vehicle and SfM photogrammetry. Drones, 4, 55.

Tonkin, T., Midgley, N., 2016. Ground-Control Networks for Image Based Surface Reconstruction: An Investigation of Optimum Survey Designs Using UAV Derived Imagery and Structure-from-Motion Photogrammetry. Remote Sensing, 8, 786.

Toth, C., Jóźków, G., 2016. Remote sensing platforms and sensors: A survey. ISPRS Journal of Photogrammetry and Remote Sensing, 115, 22-36.

Vacca et al., 2017. The Use of Nadir and Oblique UAV Images for Building Knowledge. Isprs International Journal of Geo Information.

Villanueva, J.K.S., Blanco, A.C., 2019. Optimization of Ground Control Point (Gcp) Configuration for Unmanned Aerial Vehicle (Uav) Survey Using Structure from Motion (Sfm). The International Archives of the Photogrammetry, Remote Sensing and Spatial Information Sciences, XLII-4/W12, 167-174.

Wackrow, R., Chandler, J.H., 2011. Minimising systematic error surfaces in digital elevation models using oblique convergent imagery. The Photogrammetric Record, 26, 16-31.

Westaway, R.M., Lane, S.N. and Hicks, D.M., 2003. Remote survey of large-scale braided rivers using digital photogrammetry and image analysis. International Journal of Remote Sensing, 24, 795-816

Wolf, P.R., Dewitt, B.A., Wilkinson, B.E., 2014. Elements of Photogrammetry with Applications in GIS. McGraw-Hill Education.